FULL PAPER

Photocatalyst Interface Engineering: Spatially Confined Growth of ZnFe₂O₄ within Graphene Networks as Excellent Visible-Light-Driven Photocatalysts

Deren Yang, Jing Feng, Lili Jiang, Xiaoliang Wu, Lizhi Sheng, Yuting Jiang, Tong Wei, and Zhuangjun Fan*

High-performance photocatalysts should have highly crystallized nanocrystals (NCs) with small sizes, high separation efficiency of photogenerated electron–hole pairs, fast transport and consumption of photon-excited electrons from the surface of catalyst, high adsorption of organic pollutant, and suitable band gap for maximally utilizing sunlight energy. However, the design and synthesis of these versatile structures still remain a big challenge. Here, we report a novel strategy for the synthesis of ultrasmall and highly crystallized graphene–ZnFe₂O₄ photocatalyst through interface engineering by using interconnected graphene network as barrier for spatially confined growth of ZnFe₂O₄, as transport channels for photon-excited electron from the surface of catalyst, as well as the electron reservoir for suppressing the recombination of photogenerated electron–hole pairs. As a result, about 20 nm ZnFe₂O₄ NCs with highly crystallized (311) plane confined in the graphene network exhibit an excellent visible-light-driven photocatalytic activity with an ultrafast degradation rate of 1.924×10^{-7} mol g^{-1} s^{-1} for methylene blue, much higher than those of previously reported photocatalysts such as spinel-based photocatalysts (20 times), TiO₂-based photocatalysts (4 times), and other photocatalysts (4 times). Our strategy can be further extended to fabricate other catalysts and electrode materials for supercapacitors and Li-ion batteries.

1. Introduction

Oxide semiconductor is a widely investigated material for the photodecomposition of organic pollutants and toxic contaminants in air and water.[1] Among them, TiO₂ has been considered as a promising photocatalyst due to outstanding stability, good photostability, nontoxicity, and low cost.[2,3] However, the disadvantage of TiO₂ photocatalyst is the requirement of UV-light irradiation for photocatalytic activation due to its large band gap (3.2 eV),[4] since UV light accounts for a small portion (5%) of the solar spectrum as compared to visible light (52%) and infrared light (43%).[5]

Recently, spinel-type complex oxides, such as MnFe₂O₄,[6] ZnFe₂O₄,[7] and NiFe₂O₄,[8] have attracted much attention due to visible-light-driven photoactivity. For example, ZnFe₂O₄ has a relatively narrow band gap of 1.9 eV, high catalytic activity, good durability, low cost, and easy magnetic separation.[9,10] It is worth noting that the catalytic properties of catalysts are highly related to their crystal sizes, crystallinity, active surface area, accessibility with pollutant, and diffusion resistance of organic molecules.[11,12] On the one hand, the small crystal sizes are generally beneficial for surface-dependent photocatalysis, leading to the enhanced reactive sites.[13] For example, the incorporation of graphene into ZnFe₂O₄ plays an important role in acting as support for grain refinement of the catalysts, as well as photogenerated electron transfer from ZnFe₂O₄ to graphene, resulting in the enhanced photoactivity.[14] On the other hand, good crystallinity has been found to favor higher photocatalytic activity. High-temperature synthesis of catalysts can effectively increase the crystallinity, however, it is inevitable to increase the grain size and decrease the surface area, thus resulting in the decreased active sites.[15] Therefore, it remains a significant challenge for obtaining highly crystallized catalysts with small grain size or high surface area. Additionally, other requirements such as high separation efficiency of photogenerated electron-hole pairs, fast transport and consumption of photon-excited electrons from the surface of catalyst, high adsorption of organic pollutant, and suitable band gap for maximally utilizing sunlight energy should also be considered for the design of high-performance photocatalysts.[16]

Here, we report a novel strategy for spatially confined growth of ZnFe₂O₄ within graphene network through interface engineering, as shown in **Figure 1**a. Ultrasmall graphene oxide (USGO) sheets derived from photo-Fenton reaction act as barriers for the confined growth of ZnFe₂O₄ during high-temperature heat treatment. Moreover, the interconnected graphene network can act as fast transport channels for photon-excited electron from the surface of catalyst, as well as electron reservoir for suppressing the recombination of photogenerated electron–hole pairs. Due to its mesoporous structure with ultrasmall grain size (20 nm), highly crystallized (311) plane, fast electron transport in

Dr. D. Yang, Prof. J. Feng, Dr. L. Jiang, Dr. X. Wu,
Dr. L. Sheng, Dr. Y. Jiang, Prof. T. Wei, Prof. Z. Fan
Key Laboratory of Superlight Materials
and Surface Technology
Ministry of Education
College of Material Science and Chemical Engineering
Harbin Engineering University
Harbin 150001, P. R. China
E-mail: fanzhj666@163.com

www.MaterialsViews.com

ADVANCED
FUNCTIONAL
MATERIALS
www.afm-journal.de

FULL PAPER
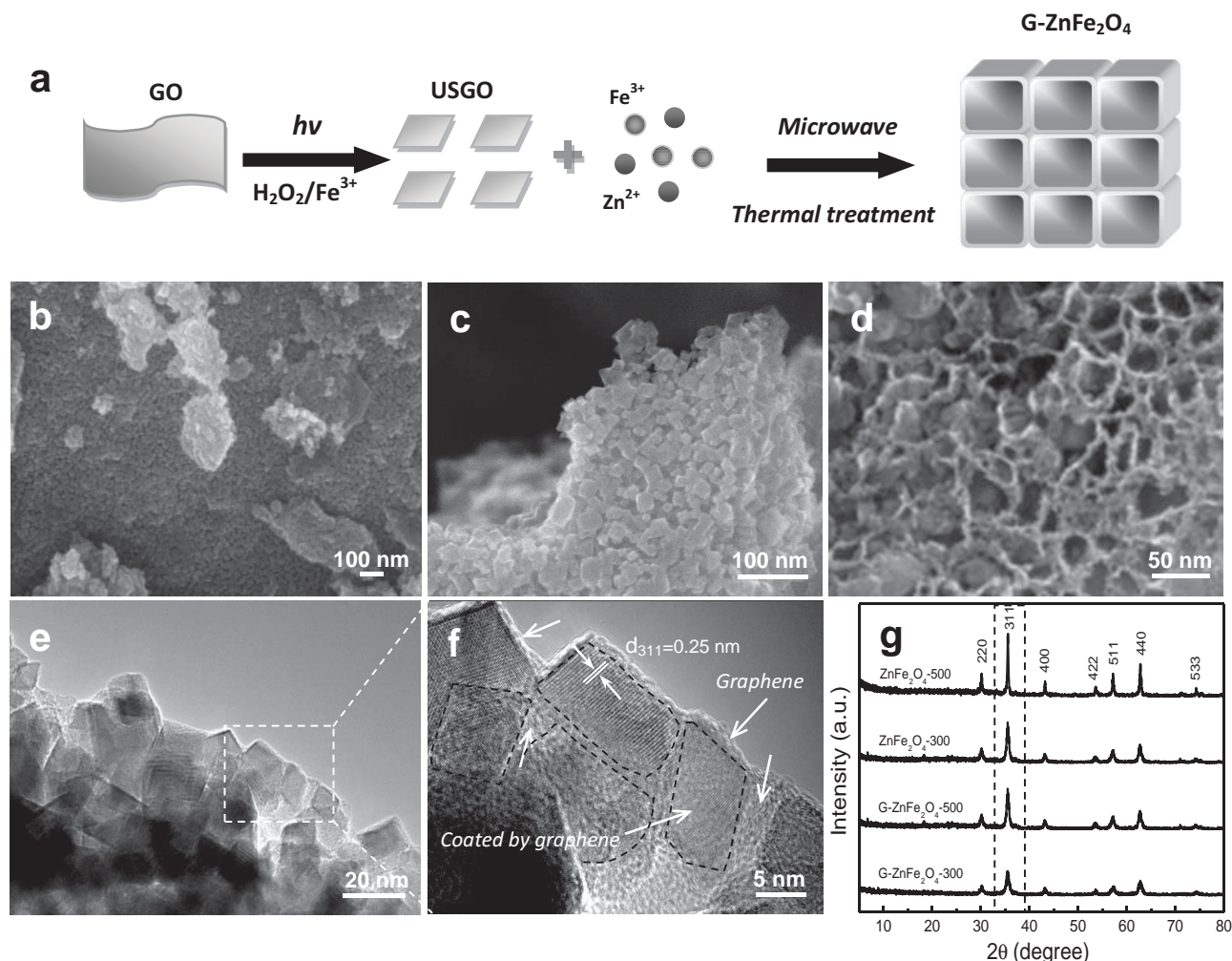
Figure 1. a) Schematic illustration of the preparation of G-ZnFe$_2$O$_4$ samples. b) SEM images of G-ZnFe$_2$O$_4$-300, c) G-ZnFe$_2$O$_4$-500, and d) the graphene conductive network in G-ZnFe$_2$O$_4$-500. e) TEM and f) HRTEM images of G-ZnFe$_2$O$_4$-500. g) XRD patterns of G-ZnFe$_2$O$_4$-300, G-ZnFe$_2$O$_4$-500, ZnFe$_2$O$_4$-300, and ZnFe$_2$O$_4$-500 (The dotted region shows obvious grain growth along (311) crystal plane compared with other crystal planes).

conductive network, and high methylene blue (MB) adsorption capability and visible-light absorption, the magnetically separable graphene–ZnFe$_2$O$_4$ catalyst shows an excellent visible-light-driven photocatalytic activity with an ultrafast degradation rate of 1.924×10^{-7} mol g$_{cat}^{-1}$ s^{-1} for MB, 20 times higher than those of previously reported spinel-based photocatalysts, TiO$_2$-based photocatalysts (4 times), and other photocatalysts (4 times).

2. Results and Discussion

Generated hydroxyl radicals (·OH) under the photoassisted catalysis of Fe^{3+}/Fe^{2+} in water can cut graphene oxide (GO) sheets into graphene oxide quantum dots.[17] In this work, photo-Fenton reaction was carried out in an 80 W UV lamp for 10 h. The obtained USGO sheets have an average lateral size of 20–50 nm (Figure S1a,b, Supporting Information). After thermal treatment of USGO/ferrite precursor at 300 °C, G-ZnFe$_2$O$_4$-300 nanoparticles exhibit the sizes of 10–15 nm (Figure 1b and Figure S2d, Supporting Information), smaller

than that of ZnFe$_2$O$_4$-300 (20 nm, Figure S2a, Supporting Information). It is worth noting that the size of USGO is comparable with the size of pure ZnFe$_2$O$_4$, suggesting that USGO sheets as barriers are very suitable for spatially confined growth of ZnFe$_2$O$_4$ during thermal treatment. Even at 500 °C, G-ZnFe$_2$O$_4$ has ultra-small ZnFe$_2$O$_4$ nanoparticles with the sizes of about 20 nm (Figure 1c and Figure S2f, Supporting Information), suggesting that the crystal growth is effectively inhibited by ultrasmall graphene nanosheets. After the partial removal of ZnFe$_2$O$_4$ for G-ZnFe$_2$O$_4$-500, it further confirms the existence of graphene network with the grid size of 20–50 nm (Figure 1d), which is beneficial for fast electron transport, resulting in the enhanced charge separation for photocatalyst. Furthermore, element mapping pattern of G-ZnFe$_2$O$_4$-500 reveals uniform distribution of zinc, iron, and oxygen, as well as carbon (Figure S2j, Supporting Information). Thermogravimetric analysis (TGA) of G-ZnFe$_2$O$_4$-500 reveals an amount of 5 wt% of carbon in the hybrid material (Figure S3, Supporting Information). To get insight into the effect of the USGO doping amounts on the structures of hybrid materials,

**ADVANCED
FUNCTIONAL
MATERIALS**

www.afm-journal.de

FULL PAPER

*Materials
Views*

www.MaterialsViews.com

the incorporation of 10 wt% USGO into G-ZnFe$_2$O$_4$ was also prepared for comparison. The G-ZnFe$_2$O$_4$-500-10 wt% hybrid material exhibits the particles size of about 20 nm (Figure S4d, Supporting Information), similar to G-ZnFe$_2$O$_4$-500, indicating that the temperature is more critical than doping concentration for adjusting the sizes of the G-ZnFe$_2$O$_4$ samples.
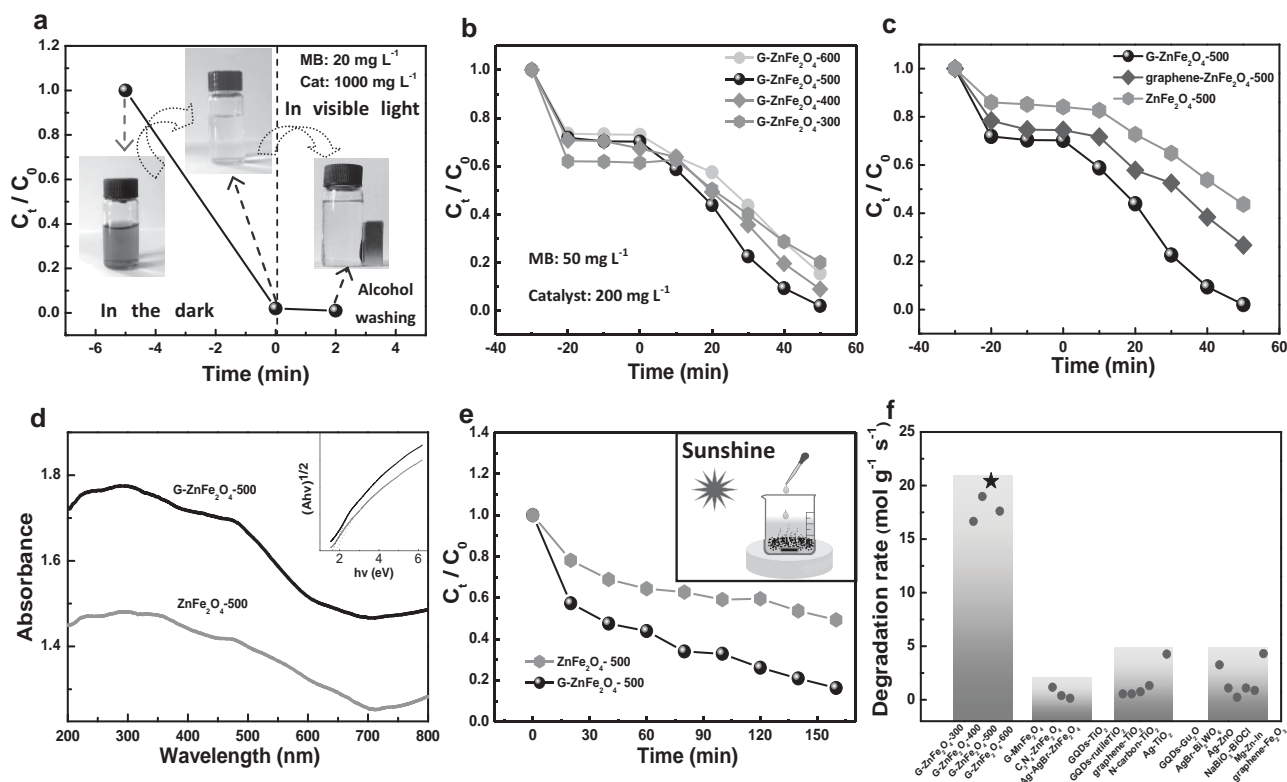
Without adding graphene nanosheets, the size distribution of ZnFe$_2$O$_4$ nanoparticles ranges from 30 to 100 nm, indicating that nanoparticles are connected with each other to form agglomerated structure after heat-treatment at 500 °C (Figure S2c, Supporting Information). More importantly, transmission electron microscope (TEM) image of G-ZnFe$_2$O$_4$-500 shows that ZnFe$_2$O$_4$ particles have cube-shaped structure with the size of about 20 nm (Figure 1e and Figure S2i, Supporting Information) due to the dimensional restriction within graphene network during the thermal-treatment. Additionally, the graphitic lattice of graphene network can be clearly observed (Figure 1f, marked by arrows). With temperatures up to 600 °C, the most grain size of G-ZnFe$_2$O$_4$-600 is larger than 50 nm due to rapid grain aggregation and growth at elevated temperature (Figure S2h, Supporting Information), but smaller than that of ZnFe$_2$O$_4$-600 (70–200 nm, Figure S2g, Supporting Information). For comparison, graphene–ZnFe$_2$O$_4$-500 was also synthesized by using different sizes of GO (100–200 nm and 1–2 μm, Figure S1c,d, Supporting Information) under the same experimental conditions. It can be seen that large ZnFe$_2$O$_4$ nanoparticles (20–50 nm) were deposited on graphene sheet (Figure S4a–c, Supporting Information), suggesting an insignificant confinement effect and the large graphene nanosheets only as templates for the growth of ZnFe$_2$O$_4$.

X-ray diffraction (XRD) patterns of as-prepared materials at different temperatures are shown in Figure 1g. The peaks at $2\theta = 30.24°$, $35.60°$, $43.28°$, $53.68°$, $57.36°$, and $62.78°$ represent (220), (311), (400), (422), (511), and (440) crystal planes of the cubic spinel ZnFe$_2$O$_4$ (JCPDS card No. 22-1012), with a space group of *Fd-3m*, respectively. There is no obvious characteristic peak (002) for graphene at 23°–24° due to its low-doping amount and high dispersion in the hybrid material. Compared G-ZnFe$_2$O$_4$-300 with G-ZnFe$_2$O$_4$-500, the obviously increased intensity for (311) diffraction peak is observed, indicating spatially confined growth within graphene network. Accordingly, it is worth mentioning that the ZnFe$_2$O$_4$ nanocrystals are enclosed by well-defined (311) crystal plane, which is in agreement with TEM observations (Figure 1f). Moreover, the full width at half maximum of the ZnFe$_2$O$_4$ diffraction peaks is reduced from 0.36 to 0.26 for (311) plane, indicating the enhanced crystallinity. As for pure ZnFe$_2$O$_4$, all intensities for diffraction peaks increase with temperature, confirming its anisotropic growth.

N$_2$ adsorption–desorption isotherm of G-ZnFe$_2$O$_4$-500 exhibits type IV isotherm with distinct H3-type hysteresis loop at a relative pressure P/P_0 of 0.45–1.0 (**Figure 2**a), indicating the existence of abundant mesopores with the sizes of 2–5 nm, which is also confirmed by pore size distribution of G-ZnFe$_2$O$_4$-500 (Figure S5a, Supporting Information).[18] Brunauer–Emmett–Teller (BET) specific surface area of G-ZnFe$_2$O$_4$-500 is 75.4 m^2 g^{-1}, 2.7 times higher than that of ZnFe$_2$O$_4$-500 (27.6 m^2 g^{-1}). More importantly, the incorporation of graphene into ZnFe$_2$O$_4$ can effectively inhibit the grain growth at temperatures <500 °C, which is further confirmed
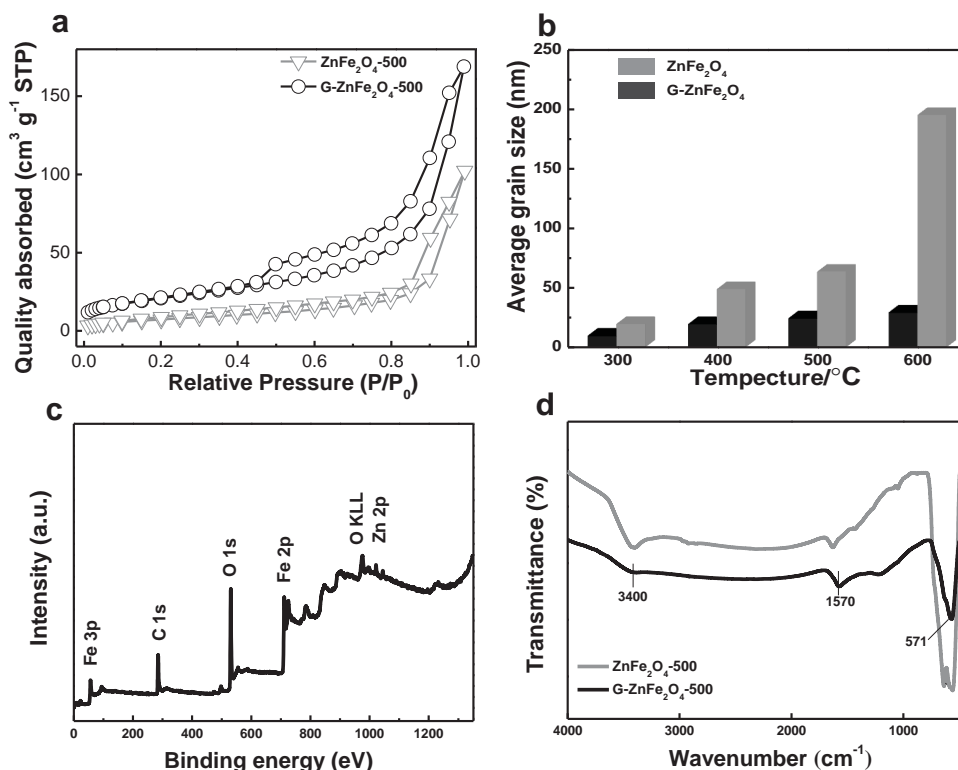
Figure 2. a) Nitrogen adsorption–desorption isotherms of G-ZnFe$_2$O$_4$-500 and ZnFe$_2$O$_4$-500. b) Average grain size of ZnFe$_2$O$_4$ and G-ZnFe$_2$O$_4$ with temperature. c) XPS spectrum of G-ZnFe$_2$O$_4$-500. d) FTIR spectrum of G-ZnFe$_2$O$_4$-500 and ZnFe$_2$O$_4$-500.

www.MaterialsViews.com

ADVANCED
FUNCTIONAL
MATERIALS
www.afm-journal.de

FULL PAPER

Figure 3. a) The photocatalytic activity of G-ZnFe$_2$O$_4$-500 in degradation of MB (catalyst: 1000 mg L^{-1}; MB: 20 mg L^{-1}). b) The photodegradation of MB using different photocatalysts under visible-light irradiation (catalyst: 200 mg L^{-1}; MB: 50 mg L^{-1}). c) Comparison of photocatalytic activity of G-ZnFe$_2$O$_4$-500 and ZnFe$_2$O$_4$-500 (catalyst: 200 mg L^{-1}; MB: 50 mg L^{-1}). d) UV–vis diffuse reflectance spectra of G-ZnFe$_2$O$_4$-500 and ZnFe$_2$O$_4$-500. Inset in panel (d) shows plots of $(A \times h\nu)^{1/2}$ versus energy ($h\nu$) for G-ZnFe$_2$O$_4$-500 and ZnFe$_2$O$_4$-500. e) The photocatalytic activities of G-ZnFe$_2$O$_4$-500 and ZnFe$_2$O$_4$-500 under solar light in Northeast China at around noon of September (catalyst: 200 mg L^{-1}; MB: 50 mg L^{-1}). f) Comparison of degradation rates with previously reported various photocatalysts.

by the grain size with temperature (Figure S6, Supporting Information). Therefore, high surface area and mesoporous channels of G-ZnFe$_2$O$_4$-500 are beneficial for the enhanced photocatalytic performances by absorbing more MB molecules, providing more reaction sites and facilitating the diffusion of pollutant and product into/out the photocatalyst.

X-ray photoelectron spectroscopy (XPS) was used to characterize the valent state of elements in G-ZnFe$_2$O$_4$-500. The survey XPS spectrum revealed the predominant presence of Zn, Fe, O, and C elements, and no other heteroelements were detected (Figure 2c). The Zn 2p XPS spectrum (Figure S7a, Supporting Information) shows two peaks at binding energies of 1044.7eV (Zn 2p$_{1/2}$) and 1021.6eV (Zn 2p$_{3/2}$), corresponding to Zn^{2+} in the crystal structure. The peaks of Fe 2p$_{1/2}$, Fe 2p$_{3/2}$ orbital of trivalent iron ions are observed at 725.0 and 711.2 eV with the shake-up satellite structure at 719.5 eV (Figure S7b, Supporting Information). Moreover, the high-resolution C1s spectrum (Figure S7c, Supporting Information) displays the strong signal of C–C at 284.6 eV, the distinguishable C—OH peak at 286.2 eV and C=O peak at 288.6 eV, revealing the removal of most oxygen containing functional groups on the graphene after thermal treatment.[19]

Figure 2d displays FTIR spectrum of G-ZnFe$_2$O$_4$-500 and ZnFe$_2$O$_4$-500. The band at 571 cm^{-1} is assigned as the symmetric stretching vibration peak of Fe—O band in the ZnFe$_2$O$_4$

structure, and 1570 cm^{-1} is the stretching vibrations of the unoxidized carbon backbone.[14,20] Obvious blueshift of the Fe–O band for the pure ZnFe$_2$O$_4$-500 has been seen after graphene doping. Thus, together with our TEM observation, the shift to lower wavenumber and the appearance of new peaks in G-ZnFe$_2$O$_4$-500 can be explained by the successful assembling between graphene and ZnFe$_2$O$_4$ nanoparticles. Compared to ZnFe$_2$O$_4$-500, the decreased adsorption peak of Fe–O band for G-ZnFe$_2$O$_4$-500 further confirms graphene-coated ZnFe$_2$O$_4$ structure. Additionally, the broad adsorption peak of G-ZnFe$_2$O$_4$-500 at 3400 cm^{-1} means little adsorption of physisorbed H$_2$O from the atmosphere, confirming its hydrophobicity character. The reduction of USGO after microwave-thermal treatment was investigated by Raman spectroscopy analysis (Figure S5b, Supporting Information). The intensity ratio (I_D/I_G) of D band to G band of the G-ZnFe$_2$O$_4$-500 is about 1.09, higher than that of USGO (0.92), meaning the presence of unrepaired defects after the removal of partial oxygen groups.[21] Moreover, I_D/I_G of USGO (0.92) is higher than that of GO (0.86), confirming that more defects are introduced during photo-Fenton reaction.

UV–vis diffuse reflectance spectra was used to determine the optical properties of the samples, as shown in **Figure 3**d. The incorporation of ultrasmall graphene sheets into ZnFe$_2$O$_4$ matrix has a significant effect on the optical property in the

ADVANCED
FUNCTIONAL
MATERIALS
www.afm-journal.de

Materials Views
www.MaterialsViews.com

FULL PAPER

visible-light absorption region. Compared to $ZnFe_2O_4$-500, G-$ZnFe_2O_4$-500 shows the enhanced visible-light absorption, meaning higher photocatalytic activity under visible-light irradiation. A plot based on the Kubelka–Munk function versus the energy of light is shown in the inset of Figure 3d. The estimated band gap value of G-$ZnFe_2O_4$-500 is 1.65 eV, lower than 1.82 eV for $ZnFe_2O_4$-500, indicating more adsorption of visible light and more photogenerated charges for G-$ZnFe_2O_4$-500, which will enhance the photocatalytic performances.

Given the excellent optical properties, the photodegradation of MB in the presence of H_2O_2 under visible-light irradiation was investigated (Figure 3a–e). When the amounts of catalyst (1000 mg L^{-1}) and organic pollutant (20 mg L^{-1}) were the same as those of previously reported parameters,[22] more interestingly, the G-$ZnFe_2O_4$-500 photocatalyst shows an ultrafast rate for the decomposition of MB within 2 min under visible-light irradiation (Figure 3a and Movie S1, Supporting Information). Moreover, almost no MB can be detected after the used catalyst was washed by ethanol, meaning that MB can be rapidly adsorbed onto the catalyst and simultaneously photodegraded. To better investigate the photocatalytic behavior of G-$ZnFe_2O_4$ catalysts, the catalyst amount was decreased by 5 times (200 mg L^{-1}), and the MB amount was increased by 2.5 times (50 mg L^{-1}) in the following experiments. Before visible-light irradiation, the mixture containing the catalyst and MB was stirred in the dark for 30 min to ensure that MB can be adsorbed onto the surface of catalysts. In the dark, the adsorption capacity of MB onto the G-$ZnFe_2O_4$ catalysts in the range from 10% to 40% of C/C_0 depends on their surface area or grain sizes (Figures 3b and 2b). Among G-$ZnFe_2O_4$ catalysts, G-$ZnFe_2O_4$-500 exhibits the best photocatalytic activity, which can completely degrade MB nearly 100% within 50 min under visible-light irradiation. Compared with $ZnFe_2O_4$-500 and graphene–$ZnFe_2O_4$-500, the degradation rate of G-$ZnFe_2O_4$-500 is much higher than that of graphene–$ZnFe_2O_4$-500, and almost two times higher than that of $ZnFe_2O_4$-500 (Figure 3c). Therefore, the improved photoactivity of G-$ZnFe_2O_4$-500 is attributed to its more reactive facets being exposed to organic dyes. For comparison, pure USGO showed a high adsorption of 72% MB and displayed little photocatalytic activity under visible-light irradiation (Figure S8, Supporting Information).

Moreover, it can be clearly seen that the activity of G-$ZnFe_2O_4$ continually increases with temperature increasing from 300 to 500 °C due to the enhanced degree of crystallinity. However, the grain size of $ZnFe_2O_4$ is overlarge at 600 °C (Figure S2h, Supporting Information), resulting in the decreased photocatalytic activity. As for pure $ZnFe_2O_4$, the photocatalytic activity of catalysts decreases with temperature due to the greatly decreased surface area or active sites (Figure 2b, Figure S9a and Table S1, Supporting Information). Although the grain size of $ZnFe_2O_4$-300 is a little bigger than that of G-$ZnFe_2O_4$-300, the photocatalytic activity of G-$ZnFe_2O_4$-300 is lower than that of $ZnFe_2O_4$-300 due to its high crystallinity for $ZnFe_2O_4$-300 (Figure S9b, Supporting Information), meaning that the degree of crystallinity is more important for the enhanced activity than grain size. Therefore, it is reasonable to expect that a good photocatalyst should be considered the balance between grain size (surface area) and crystallinity.

Figure 3f shows the comparison of the degradation rate for organic pollutants using different photocatalysts. The degradation rate (v) of the catalyst can be defined as

$$v = \frac{1}{m_{cat}} \times \frac{dn}{dt} \tag{1}$$

where n is the amount of organic pollutants (mol), m is the mass of catalyst (g_{cat}), and t is reaction time (s). It is can be seen that the degradation rate of G-$ZnFe_2O_4$-500 is 1.924×10^{-7} mol g_{cat}^{-1} s^{-1}, almost 20 times higher than those of previously reported spinel-based photocatalysts,[9,23] 4 times higher than those of TiO_2-based photocatalysts,[3,24] and other photocatalysts,[25] holding a great promising application for environmental protection. To better evaluate the photocatalytic ability of photocatalysts, it is reasonable for applying degradation rate as an important parameter for the real application.

In order to simulate real-world reaction conditions, the G-$ZnFe_2O_4$-500 and $ZnFe_2O_4$-500 catalysts were tested in the solar light. More interestingly, under the conditions of low catalyst loading (200 mg L^{-1}) and high MB concentration (50 mg L^{-1}), almost 84% of MB is photodegraded within 160 min, compared with 50% for $ZnFe_2O_4$-500 (in northeast China at around noon of September). Although the degradation rate of G-$ZnFe_2O_4$-500 in the solar light is 4 times slower than that in a 300 W Xe lamp, it is worth mentioning that G-$ZnFe_2O_4$-500 is a promising catalyst for real application in the photodegradation of organic pollutants.

The magnetic property of the G-$ZnFe_2O_4$-500 hybrid material was investigated using a vibrating sample magnetometer (VSM, JDM-14D) at 300 K in an applied magnetic field up to 10 000 Oe (**Figure 4**a). The G-$ZnFe_2O_4$-500 photocatalyst shows ferromagnetic property with a saturation magnetization (Ms) of 42.1 emu g^{-1}, which is quite qualified for the magnetic separation and recycling of photocatalysts. As demonstrated in the inset of Figure 4a, complete separation of the catalyst colloids from the solution can be achieved within 1 min under an external magnetic field (0.3 T). After that, we further investigated the stability and reusability of G-$ZnFe_2O_4$-500 photocatalyst by collecting and reusing the photocatalyst for five cycles (Figure 4b). There is a little loss in the photocatalytic activity due to the loss of photocatalyst during each round of collection and rinsing.
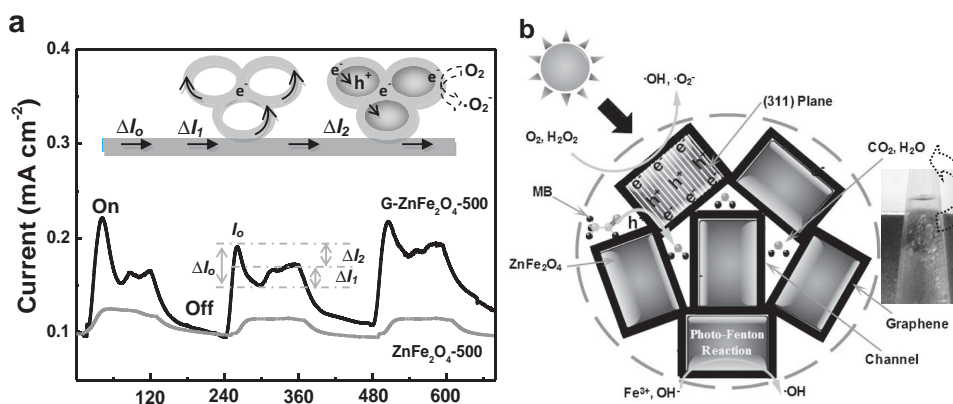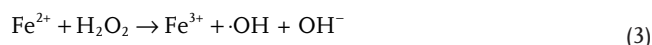
Figure S10a (Supporting Information) shows the photocatalytic performances of G-$ZnFe_2O_4$-500 with or without H_2O_2 under visible-light irradiation or in the dark. It is clearly seen that G-$ZnFe_2O_4$-500 can completely degrade MB nearly 100% within 50 min in the presence of H_2O_2 under visible-light irradiation. Whereas G-$ZnFe_2O_4$-500 only shows an adsorption of 30% MB and displays little degradation with or without H_2O_2 in the dark, meaning that the degradation of MB is mainly attributed to the photocatalysis. Compared with $ZnFe_2O_4$-500 and graphene-$ZnFe_2O_4$-500, it should be noticed that G-$ZnFe_2O_4$-500 without H_2O_2 also exhibits the highest photocatalytic activity with the degradation of 85% MB within 70 min under visible-light irradiation (Figure S10b, Supporting Information), further confirming that the interconnected conductive graphene network is more beneficial to the fast electron transport than graphene sheets.

www.MaterialsViews.com

**ADVANCED
FUNCTIONAL
MATERIALS**
www.afm-journal.de

FULL PAPER

a

b
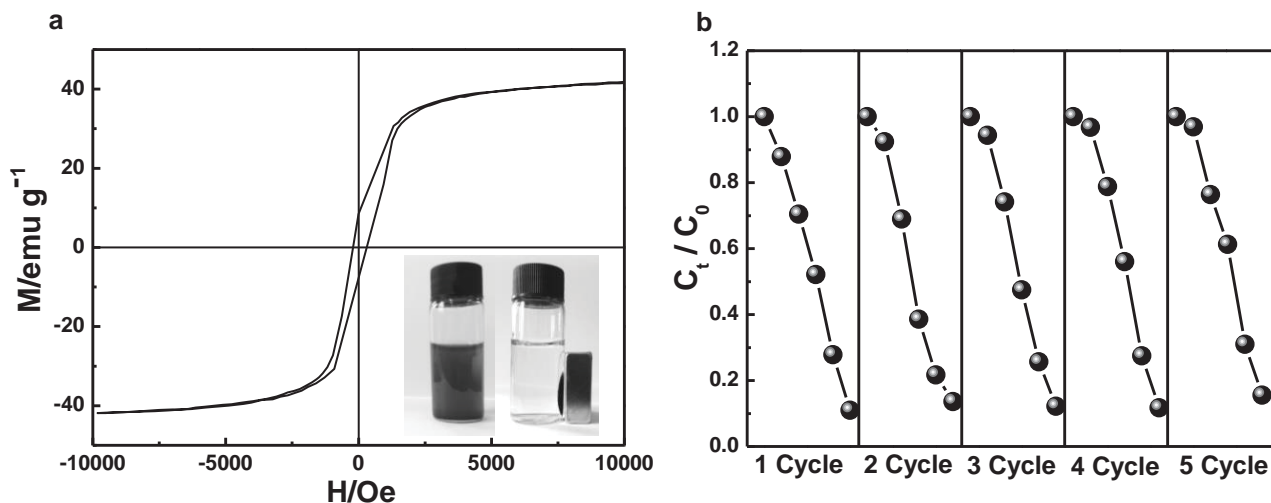
Figure 4. a) The hysteresis loop of G-ZnFe$_2$O$_4$-500 measured at room temperature. The inset shows the image of G-ZnFe$_2$O$_4$-500 suspension without (left) and with a magnetic field (right). b) Five cycles using G-ZnFe$_2$O$_4$-500 photocatalyst under visible-light irradiation for 50 min.

To investigate the transfer efficiency of photogenerated electrons of G-ZnFe$_2$O$_4$-500 and ZnFe$_2$O$_4$-500, the transient photocurrent response curves were measured under several on-off cycles of intermittent visible-light irradiation (**Figure 5**a). It is notable that G-ZnFe$_2$O$_4$-500 exhibits stronger transient photocurrent response, about three times larger than that of ZnFe$_2$O$_4$-500, indicating higher transfer efficiency of photogenerated electrons and separation efficiency of photogenerated electron–hole pairs.[26] The photocurrent of G-ZnFe$_2$O$_4$-500 rapidly transfers from carbon surface to current collector as shown in the inset of Figure 5a, consequently, the loss of photocurrent (ΔI_o) consists of the injection of charges into graphene network (ΔI_1), and the consumption of electrons (ΔI_2) including the reaction between electrons and O$_2$ and the recombination of electron–hole pairs. Therefore, separation efficiency of photogenerated electron–hole pairs is effectively improved by the consumption of photon-excited electrons stored in the graphene networks. The photocatalytic activity can also be determined by the difference between of the position of conduction band (CB) and valence band (VB),[27] as shown in Figure S11 (Supporting Information). Under visible-light irradiation, the photogenerated electrons are migrated from the VB of ZnFe$_2$O$_4$ to the CB, leaving the holes in the VB of ZnFe$_2$O$_4$. The CB of ZnFe$_2$O$_4$ is more negative than the O$_2$/·O$_2^-$ redox couple, indicating that the photogenerated electrons injected into graphene network can react with O$_2$/H$_2$O$_2$ to produce ·O$_2^-$/·OH with strong oxidizing property. Moreover, the holes in the VB of ZnFe$_2$O$_4$ can directly react with MB. Apart from photocatalysis, Fenton reaction and photo-Fenton reaction can also participate in MB degradation process.[14,28]

$$Fe^{3+} + e^- \rightarrow Fe^{2+} \tag{2}$$

$$Fe^{2+} + H_2O_2 \rightarrow Fe^{3+} + ·OH + OH^- \tag{3}$$

$$Fe^{3+} + h\nu + OH^- \rightarrow Fe^{2+} + ·OH \tag{4}$$

a

b

Figure 5. a) The photocurrent responses of G-ZnFe$_2$O$_4$-500 and ZnFe$_2$O$_4$-500 in 0.5 M Na$_2$SO$_4$ electrolyte under visible-light irradiation. The inset represents the charge transfer process. b) Schematic photocatalytic reaction process and charge transfer for G-ZnFe$_2$O$_4$-500. The inset shows the image of a lot of bubbles (degradation product) generated by photocatalyst under visible-light irradiation when G-ZnFe$_2$O$_4$-500 suspension was taken out at a given time interval.

Based on the above experiment results, the excellent photocatalytic performances of G-ZnFe$_2$O$_4$ are attributed to its unique structure, as shown in Figure 5b. First, MB can be easily and rapidly adsorbed onto G-ZnFe$_2$O$_4$ catalyst due to its high surface area and mesoporous structure. After that, small crystallite size with more active sites and high crystallinity of catalyst are beneficial for the photodegradation, resulting in high photocatalytic activity.[11] Second, owing to the π–π conjugated structure, graphene layer on ZnFe$_2$O$_4$ particles can enhance the adsorption capability for organic dyes and visible-light absorption, which is beneficial to the acceleration of photocatalytic reaction. Third, these photon-excited electrons can freely transfer from catalyst surface through 3D interconnected conductive graphene network. Additionally, graphene network can serve as electron reservoir that can suppress the recombination of photogenerated electron–hole pairs, and mesoporous channels can facilitate the diffusion of pollutant and product into photocatalyst, accelerating the photocatalytic reaction.[29] Finally, the photogenerated holes and active oxygen radicals (such as O$_2^-$ and OH) generated from both photogenerated electrons and photo-Fenton reaction exhibit strong degradation of organic dyes.[14,30]

3. Conclusion

In summary, we report a novel strategy for spatially confined growth of ZnFe$_2$O$_4$ within graphene network by interface engineering. The interconnected graphene network in the hybrid is beneficial for spatially confined growth of ZnFe$_2$O$_4$ and fast transport of photon-excited electron from catalyst surface, and it also acts as electron reservoir that can suppress the recombination of photogenerated electron-hole pairs. Moreover, the magnetically separable graphene–ZnFe$_2$O$_4$ catalyst shows excellent photodegradation ability with an ultrafast rate of 1.924×10^{-7} mol g$_{cat}^{-1}$ s^{-1}, much higher than those of previously reported photocatalysts. The findings of this work open up new opportunities for maximizing photoreactivity through microstructural control of photocatalysts.

4. Experimental Section

Synthesis of USGO Sheet: USGO sheet was synthesized by a new and facile photo-Fenton method. In a typical experiment, 100 mL of 0.5 mg mL^{-1} GO (modified Hummers method[31]) aqueous suspension, 33.3 mL of 240×10^{-3} M H$_2$O$_2$, and 2 mL of 1×10^{-3} M FeCl$_3$ aqueous solution were mixed in a glass garden under magnetic stirring for 1 h. The photo-Fenton reaction was carried out in a photoreactor equipped with an 80 W UV lamp. The distance between the light source and solution was about 5 cm. After UV light irradiation for 5 and 10 h, the obtained USGO solution was wine red, and the concentration of USGO was about 5×10^{-4} g mL^{-1}.

Synthesis of G-ZnFe$_2$O$_4$ and ZnFe$_2$O$_4$: The G-ZnFe$_2$O$_4$ samples were prepared by microwave thermal treatment. Briefly, 0.25 g polyethylene glycol, 2.02 g Fe(NO$_3$)$_3$·9H$_2$O, and 0.7437 g Zn(NO$_3$)$_2$·6H$_2$O were dissolved into 15 mL of distilled water under vigorous stirring for 30 min. Then, 60 mL of sodium acetate solution (NaAc, 0.5 g mL^{-1}) was dripped into the above solution and kept continuously stirring for 30 min until a dark brown suspension was formed. After that, 64 mL of as-prepared USGO suspension (5×10^{-4} g mL^{-1}) was added into the above solution slowly and sonicated for 20 min. The resulting suspension was

heated using a microwave oven (Haier, 2450 MHz, 700 W) for 6 min. Subsequently, the suspension was filtrated and washed thoroughly with distilled water and ethanol several times, and then dried at 120 °C for 10 h. The obtained mixture was grinded manually using an agate mortar for further thermal treatment. Finally, a series of samples were heated at 300, 400, 500 and 600 °C in N$_2$ atmosphere for 2 h, respectively, and named as G-ZnFe$_2$O$_4$-x, where x referred to treated temperature. For comparison, pure ZnFe$_2$O$_4$ and graphene–ZnFe$_2$O$_4$ with different sizes of GO were also prepared by using a similar process.

Material Characterization: The as-prepared samples were characterized by scanning electron microscope (SEM, Camscan Mx2600FE), transmission electron microscope (TEM, JEM 2010), atomic force microscope (AFM, CSPM5500 Scanning Probe Microscope), X-ray diffraction (XRD, TTR-III), X-ray photoelectron spectroscopy (XPS, PHI-5700), and VSM (JDM-14D). The BET surface areas of the samples were measured at 77 K using NOVA 2000 (Quantachrome, USA). TGA of the sample was performed on a Pyris Diamond TG/DTA thermogravimetric analyzer (Perkin-Elmer Thermal Analysis) at a heating rate of 10 °C min^{-1} from room temperature to 800 °C under air flow. FTIR spectroscopy was carried out on a Perkin-Elmer Spectrum 100 spectrometer in a range of 450–4000 cm^{-1}. UV–vis diffuse reflectance spectra were obtained using a UV–vis spectrophotometer (UV-3600, Shimadzu).

Photocatalytic Performance Measurements: The photocatalytic properties of as-obtained samples were evaluated by measuring the degradation of MB under visible-light irradiation. A 300 W xenon lamp with 420 nm filter was used as visible-light source. In a typical process, 20 mg of photocatalyst was added into 100 mL of 50 mg L^{-1} MB solution. Before irradiation, the suspensions were stirred in the dark for 30 min to ensure the establishment of adsorption–desorption equilibrium. After adding 0.5 mL of 30% H$_2$O$_2$ into the above suspensions, the cylindrical quartz vessel was exposed to the visible irradiation under ambient conditions and stirring. The distance between the light source and solution was about 10 cm. 3 mL sample solution was taken out at a given time interval during the experiment and magnetically separated to remove the catalyst completely. The absorbance changes of MB were analyzed by UV–vis spectroscopic measurements (721 UV-Visible Spectrophotometer, China) at $\lambda_{max} = 655$ nm. In the durability test of the catalyst for the photodegradation of MB under visible light, five consecutive cycles were tested, and the photocatalysts were washed thoroughly with water and dried after each cycle. The photocatalytic degradation efficiency of MB was calculated by the formula $E = \dfrac{C_0 - C_t}{C_0} \times 100\%$, where C_0 was the adsorption equilibrium absorbance of MB and C_t was the absorbance of MB solution at irradiation time (t). Photoelectrochemical experiment was performed in a standard three-electrode system with a platinum wire as the auxiliary electrode and a saturated calomel electrode (SCE) as the reference electrode. The anodes were obtained by dip-coating of G-ZnFe$_2$O$_4$-500 and ZnFe$_2$O$_4$-500 onto ITO glass, and then annealed at 400 °C for 1 h under N$_2$. A 300 W xenon lamp with a 420 nm cutoff filter was used as a visible-light source. The photocurrents were measured under visible-light irradiation with light ON–OFF switches of 120 s at a bias of 0.5 V.

Supporting Information

Supporting Information is available from the Wiley Online Library or from the author.

Acknowledgements

www.MaterialsViews.com

ADVANCED
FUNCTIONAL
MATERIALS
www.afm-journal.de

FULL PAPER

[1] a) Q. Xiang, J. Yu, M. Jaroniec, *Chem. Soc. Rev.* **2012**, *41*, 782; b) C. Chen, W. Ma, J. Zhao, *Chem. Soc. Rev.* **2010**, *39*, 4206; c) L. Jing, W. Zhou, G. Tian, H. Fu, *Chem. Soc. Rev.* **2013**, *42*, 9509.

[2] a) W. Guo, F. Zhang, C. Lin, Z. L. Wang, *Adv. Mater.* **2012**, *24*, 4761; b) C. Chen, P. Li, G. Wang, Y. Yu, F. Duan, C. Chen, W. Song, Y. Qin, M. Knez, *Angew. Chem., Int. Ed.* **2013**, *52*, 9196; c) W. Zhou, W. Li, J. Q. Wang, Y. Qu, Y. Yang, Y. Xie, K. Zhang, L. Wang, H. Fu, D. Zhao, *J. Am. Chem. Soc.* **2014**, *136*, 9280.

[3] a) J. S. Lee, K. H. You, C. B. Park, *Adv. Mater.* **2012**, *24*, 1084; b) S. Zhuo, M. Shao, S.-T. Lee, *ACS Nano* **2012**, *6*, 1059.

[4] a) S. N. Habisreutinger, L. Schmidt-Mende, J. K. Stolarczyk, *Angew. Chem., Int. Ed.* **2013**, *52*, 7372; b) H. Kisch, *Angew. Chem., Int. Ed.* **2013**, *52*, 812.

[5] L. L. Tan, S. P. Chai, A. R. Mohamed, *ChemSusChem* **2012**, *5*, 1868.

[6] M. Pal, R. Rakshit, K. Mandal, *ACS Appl. Mater. Interfaces* **2014**, *6*, 4903.

[7] S. Zhang, J. Li, M. Zeng, G. Zhao, J. Xu, W. Hu, X. Wang, *ACS Appl. Mater. Interfaces* **2013**, *5*, 12735.

[8] S. Xu, W. Shangguan, J. Yuan, M. Chen, J. Shi, *Appl. Catal., B* **2007**, *71*, 177.

[9] Y. Yao, Y. Cai, F. Lu, J. Qin, F. Wei, C. Xu, S. Wang, *Ind. Eng. Chem. Res.* **2014**, *53*, 17294.

[10] a) L. Sun, R. Shao, L. Tang, Z. Chen, *J. Alloys Compd.* **2013**, *564*, 55; b) J. H. Kim, J. H. Kim, J.-W. Jang, J. Y. Kim, S. H. Choi, G. Magesh, J. Lee, J. S. Lee, *Adv. Energy Mater.* **2015**, *5*, 1401933.

[11] a) Y. Bi, S. Ouyang, N. Umezawa, J. Cao, J. Ye, *J. Am. Chem. Soc.* **2011**, *133*, 6490; b) J. B. Joo, Q. Zhang, M. Dahl, I. Lee, J. Goebl, F. Zaera, Y. Yin, *Energy Environ. Sci.* **2012**, *5*, 6321.

[12] H. Liu, J. B. Joo, M. Dahl, L. Fu, Z. Zeng, Y. Yin, *Energy Environ. Sci.* **2015**, *8*, 286.

[13] H. Tong, S. Ouyang, Y. Bi, N. Umezawa, M. Oshikiri, J. Ye, *Adv. Mater.* **2012**, *24*, 229.

[14] Y. Fu, X. Wang, *Ind. Eng. Chem. Res.* **2011**, *50*, 7210.

[15] K. Kiatkittipong, J. Scott, R. Amal, *ACS Appl. Mater. Interfaces* **2011**, *3*, 3988.

[16] a) H. Zhou, Y. Qu, T. Zeid, X. Duan, *Energy Environ. Sci.* **2012**, *5*, 6732; b) Y. H. Ng, S. Ikeda, M. Matsumura, R. Amal, *Energy Environ. Sci.* **2012**, *5*, 9307; c) C. Huang, C. Li, G. Shi, *Energy Environ. Sci.* **2012**, *5*, 8848.

[17] X. Zhou, Y. Zhang, C. Wang, X. Wu, Y. Yang, B. Zheng, H. Wu, S. Guo, J. Zhang, *Acs Nano* **2012**, *6*, 6592.

[18] C. Long, X. Chen, L. Jiang, L. Zhi, Z. Fan, *Nano Energy* **2015**, *12*, 141.

[19] J. Yan, J. Liu, Z. Fan, T. Wei, L. Zhang, *Carbon* **2012**, *50*, 2179.

[20] A. Meidanchi, O. Akhavan, *Carbon* **2014**, *69*, 230.

[21] a) S. Stankovich, D. A. Dikin, R. D. Piner, K. A. Kohlhaas, A. Kleinhammes, Y. Jia, Y. Wu, S. T. Nguyen, R. S. Ruoff, *Carbon* **2007**, *45*, 1558; b) Y. Fu, H. Chen, X. Sun, X. Wang, *Appl. Catal., B* **2012**, *111*, 280.

[22] a) Y. Sang, Z. Zhao, M. Zhao, P. Hao, Y. Leng, H. Liu, *Adv. Mater.* **2015**, *27*, 363; b) J. Tian, Y. Sang, G. Yu, H. Jiang, X. Mu, H. Liu, *Adv. Mater.* **2013**, *25*, 5075.

[23] a) Y. Fu, P. Xiong, H. Chen, X. Sun, X. Wang, *Ind. Eng. Chem. Res.* **2012**, *51*, 725; b) X. Li, D. Tang, F. Tang, Y. Zhu, C. He, M. Liu, C. Lin, Y. Liu, *Mater. Res. Bull.* **2014**, *56*, 125.

[24] a) X. Yu, J. Liu, Y. Yu, S. Zuo, B. Li, *Carbon* **2014**, *68*, 718; b) J. Matos, M. Hofman, R. Pietrzak, *Carbon* **2013**, *54*, 460; c) J. Fei, J. Li, *Adv. Mater.* **2015**, *27*, 314.

[25] a) S. Guo, G. Zhang, Y. Guo, J. C. Yu, *Carbon* **2013**, *60*, 437; b) H. Li, R. Liu, Y. Liu, H. Huang, H. Yu, H. Ming, S. Lian, S.-T. Lee, Z. Kang, *J. Mater. Chem.* **2012**, *22*, 17470; c) D. Wang, L. Guo, Y. Zhen, L. Yue, G. Xue, F. Fu, *J. Mater. Chem. A* **2014**, *2*, 11716; d) H. Bouzid, M. Faisal, F. A. Harraz, S. A. Al-Sayari, A. A. Ismail, *Catal. Today* **2015**, *252*, 20; e) X. Chang, G. Yu, J. Huang, Z. Li, S. Zhu, P. Yu, C. Cheng, S. Deng, G. Ji, *Catal. Today* **2010**, *153*, 193; f) L. Huang, S. Chu, J. Wang, F. Kong, L. Luo, Y. Wang, Z. Zou, *Catal. Today* **2013**, *212*, 81.

[26] a) J. Zhang, M. Zhang, C. Yang, X. Wang, *Adv. Mater.* **2014**, *26*, 4121; b) C.-W. Yen, L.-K. Chu, M. A. El-Sayed, *J. Am. Chem. Soc.* **2010**, *132*, 7250; c) C. M. McShane, K.-S. Choi, *J. Am. Chem. Soc.* **2009**, *131*, 2561.

[27] a) Q. Li, X. Li, S. Wageh, A. A. Al-Ghamdi, J. Yu, *Adv. Energy Mater.* **2015**, *5*, 1500010; b) R. Dom, R. Subasri, K. Radha, P. H. Borse, *Solid State Commun.* **2011**, *151*, 470; c) P. P. Hankare, R. P. Patil, A. V. Jadhav, K. M. Garadkar, R. Sasikala, *Appl. Catal., B* **2011**, *107*, 333; d) X. Guo, H. Zhu, Q. Li, *Appl. Catal., B* **2014**, *160*, 408; e) R. Dom, R. Subasri, N. Y. Hebalkar, A. S. Chary, P. H. Borse, *RSC Adv.* **2012**, *2*, 12782; f) L. Kong, Z. Jiang, T. Xiao, L. Lu, M. O. Jones, P. P. Edwards, *Chem. Commun.* **2011**, *47*, 5512.

[28] a) O. Akhavan, *Appl. Surf. Sci.* **2010**, *257*, 1724; b) O. Akhavan, R. Azimirad, *Appl. Catal., A* **2009**, *369*, 77.

[29] Z. Gan, X. Wu, M. Meng, X. Zhu, L. Yang, P. K. Chu, *ACS Nano* **2014**, *8*, 9304.

[30] Y. Hou, X. Li, Q. Zhao, G. Chen, *Appl. Catal., B* **2013**, *142*, 80.

[31] a) X. Wu, L. Jiang, C. Long, T. Wei, Z. Fan, *Adv. Funct. Mater.* **2015**, *25*, 1648; b) L. Jiang, L. Sheng, C. Long, T. Wei, Z. Fan, *Adv. Energy Mater.* **2015**, *5*, 1500771.